Mo-doped/Ni-supported $ZnIn_2S_4$ wrapped $NiMoO_4$ S-scheme heterojunction photocatalytic reforming of lignin into hydrogen

Hang Su[a], Cheng Rao[a], Lan Zhou[a], Yuxia Pang[a], Hongming Lou[a,b,*], Dongjie Yang[a], Xueqing Qiu[c]

[a] School of Chemistry and Chemical Engineering, Guangdong Provincial Key Lab of Green Chemical Product Technology, South China University of Technology, Guangzhou, China

[b] State Key Laboratory of Pulp and Paper Engineering, South China University of Technology, Guangzhou, China

[c] School of Chemical Engineering and Light Industry, Guangdong University of Technology, Guangzhou, China

Corresponding author:

[*]E-mail address: cehmlou@scut.edu.cn (H. Lou).

Experimental Methods

Characterization

The morphologies and microstructures of the samples were examined by scanning electron microscopy (SEM, SU8220, Hitachi) and transmission electron microscopy (TEM, JEM-2100F, JEOL, equipped with an energy dispersive spectroscopy). X-ray diffraction (XRD) patterns were recorded by Bruker D8 advance X-ray diffractometer using Cu Kα radiation in the region of 2θ =5-80° at 40 kV and 20 mA. Brunauer-Emmett-Teller (BET) specific surface area of all samples was obtained by N_2 adsorption-desorption at 77 K (TristarII3flex, Micrometrics). X-ray photoelectron spectroscopy (XPS, Axis Ultra, Kratos Analytical Ltd.) measurements were performed to determine valence state of element samples. Ultraviolet photoelectron spectroscopy measurement (hν=21.2 eV), a bias of -10 V was applied to the sample to avoid interference of the spectrometer threshold in the UV photoelectron spectra. Photoluminescence (PL) spectra and time-resolved PL decay spectra were recorded on an Edinburgh FI/FSTCSPC 920 spectrophotometer under the excitation wavelength of 320 nm at room temperature. Fourier-transform infrared (FTIR) spectra were conducted on a Thermo Scientific Nicolrt IS50 spectrophotometer. Ultraviolet-visible diffuse reflectance spectra (UV-vis DRS) were collected on a Varian Cary 5000 Scan UV-vis spectrometer with $BaSO_4$ as the reference. Electron paramagnetic resonance (EPR) measurements were carried out on a Bruker model A300 spectrometer. Atomic Force Microscopy (AFM) and Kelvin Probe Force Microscopy (KPFM) was carried to analyze the structure imaging and surface potential (Bruker, Dimension ICON).

Photoelectrochemical measurements

Electrochemical measurements were carried out on an electrochemical workstation (CHI660E, Chenhua, Shanghai). electrochemical system in a standard three-electrode cell, using the prepared samples as the working electrodes with an active area of 1.0 cm^2, a Pt plate as the counter electrode and an Hg/HgCl electrode (saturated KCl) as

the reference electrode. Na_2SO_4 (0.2 M) aqueous solution was used as the electrolyte, $E_{(vs\ NHE)} = E_{fb} - E_{Hg_2Cl_2} + 0.059 \times pH$.

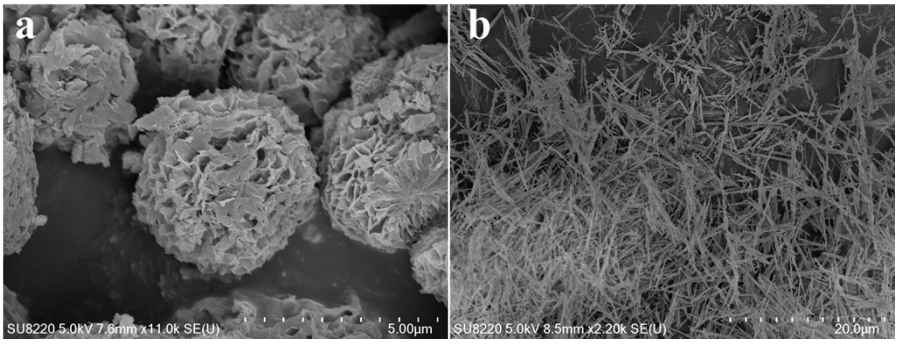

Fig. S1 SEM of (a) ZIS and (b) NMO.

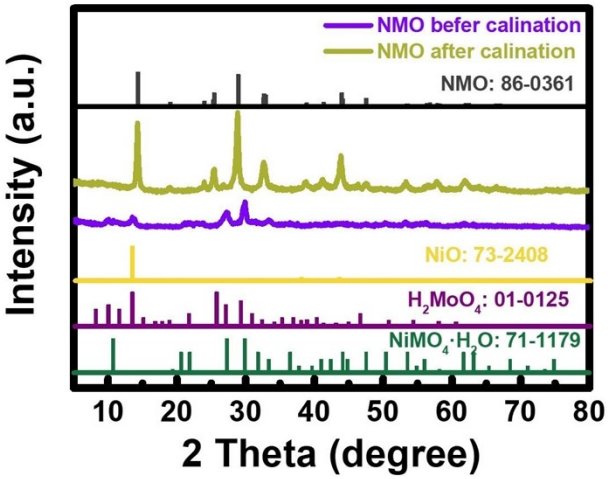

Fig. S2 XRD patterns of $NiMoO_4$ before and after calcination.

It can be seen from the **Fig. S2** that the calcination process is not to improve the crystal form, but to converts from NiO and H_2MoO_4 to NMO.

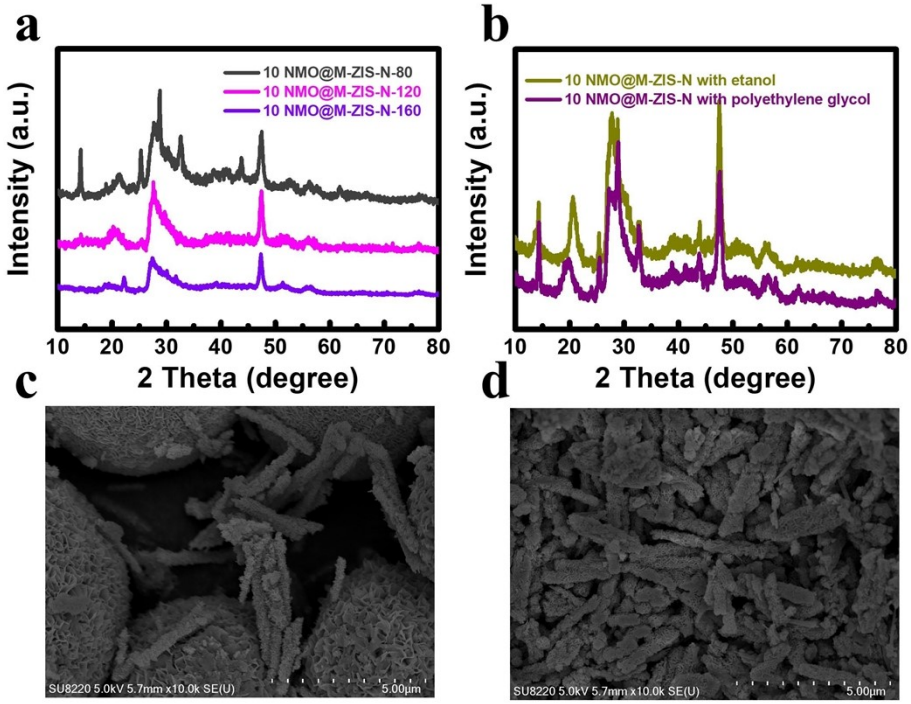

Fig. S3 XRD patterns of 10 NMO-M-ZIS-N with different temperature (a) and with different solvent (b), SEM images of 10 NMO@M-ZIS-N with ethanol (c) and with polyethylene glycol (d).

It can be seen from **Fig. S3a** that the diffraction peaks of NMO gradually disappear with the increase of temperature, which is mainly due to the dissolution of NMO, so that it is supported in the structure of ZIS in the form of Mo doping and Ni deposition. **Fig. S3b** can confirm that the composite structure of NMO@M-ZIS-N can also be synthesized by different alcohol solvents, and the corresponding SEM images are shown in **Fig. S3b**.

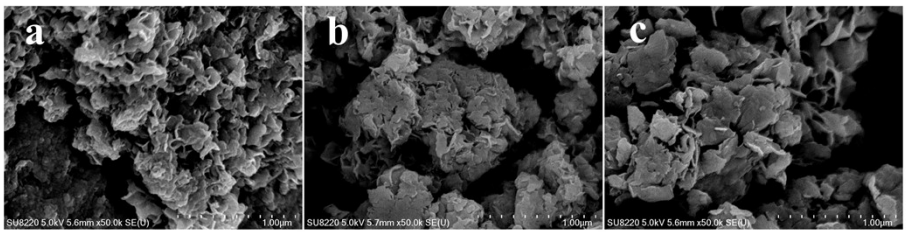

Fig. S4 SEM images of (a) M-ZIS, (b) ZIS-N and (c) M-ZIS-N.

As can be seen from **Fig. S4**, compared with the morphologies of ZIS (**Fig. S1**), the morphologies size of Mo-ZIS (M-ZIS), Mo-ZIS-Ni (M-ZIS-N) and ZIS-Ni (ZIS-N) is significantly smaller, but it is still a flower-like structure composed of agglomeration of nanosheets.

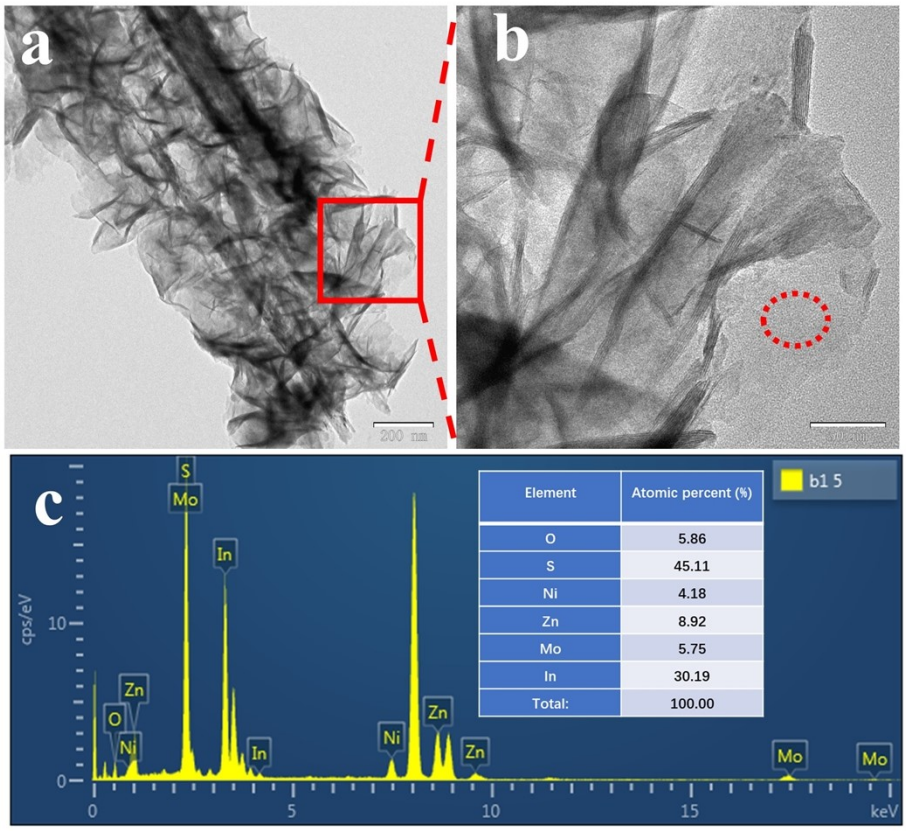

Fig. S5 TEM images of (a-b)10 NMO@M-ZIS-N and (c) corresponding EDX of 10 NMO@M-ZIS-N.

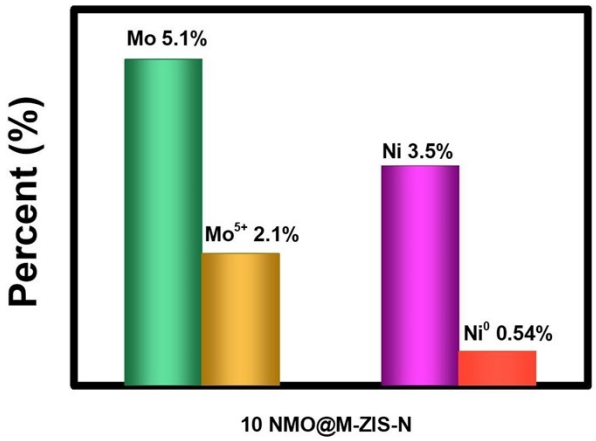

Fig. S6 Mo doping and Ni loading content in the optimized sample.

Through the XPS test, the atomic percentage of the sample can be obtained, such as Mo (5.2%), Ni (3.5%), O (22.6%), In (19.3%), Zn (9.1%), and S (40.3%). According to the ratio of the peak area of Ni deposition to Ni^{2+} peak area and the ratio of Mo^{5+} peak area to Mo^{6+} peak area, we can approximate the content of Ni deposition (0.54%) and Mo doping (2.1%).

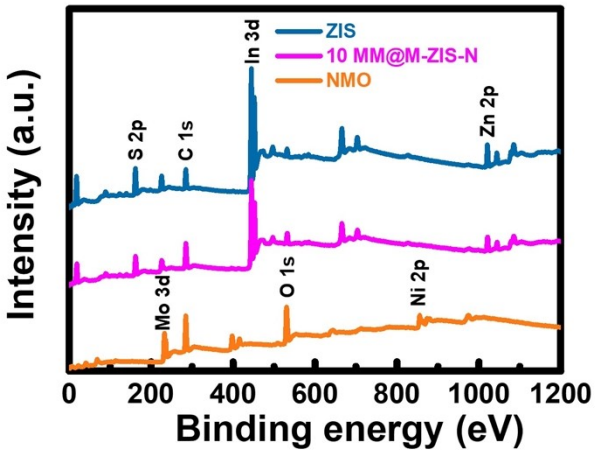

Fig. S7 XPS spectra of samples

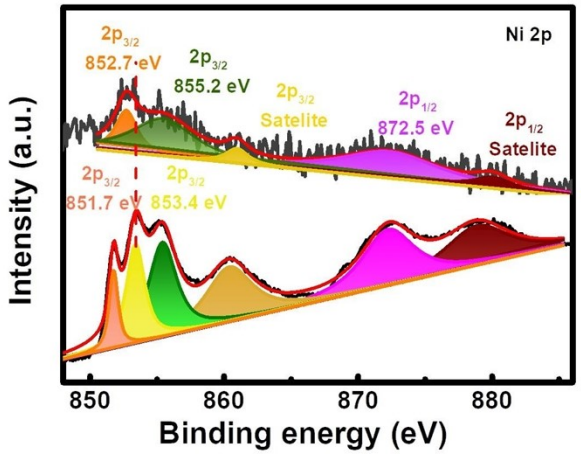

Fig. S8 Ni 2p of nickel foam.

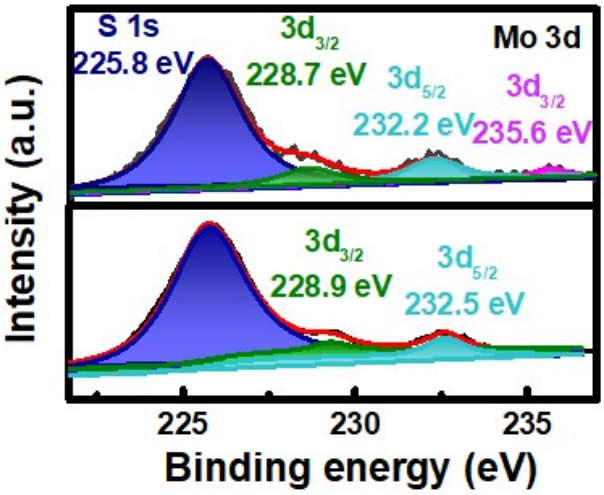

Fig. S9 XPS spectra of Mo 3d for 10 NMO@ZIS (top) and Mo-ZIS (down).

The synthesis method of Mo doped ZIS (Mo-ZIS) is the same as NMO@M-ZIS-N,

which was replaced NMO with $(NH_4)_6Mo_7O_{24}\cdot 4H_2O$.

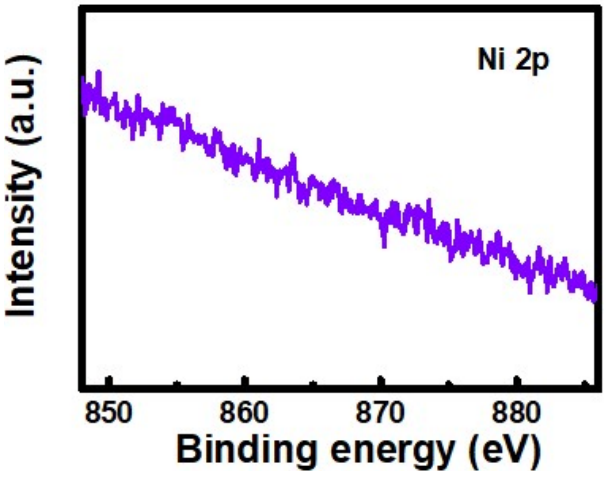

Fig. S10 XPS spectra of 4.0% Ni-ZIS

The synthesis method of Ni doped ZIS (Ni-ZIS) is the same as NMO@M-ZIS-N, which was replaced NMO with $Ni(CH_3COO)_2$.

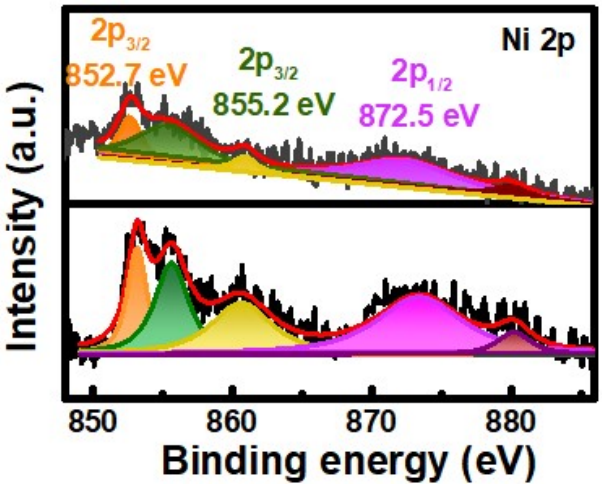

Fig. S11 XPS spectra of Ni 2p for 10 NMO@ZIS (top) and 10 NO@ZIS-N (down).

The synthesis method of Ni doped ZIS (Ni-ZIS) is the same as NMO@M-ZIS-N, which was replaced NMO with NiO, indicating the formation of metal Ni loading ZIS wrapped NiO, consistent with the previous report.[1]

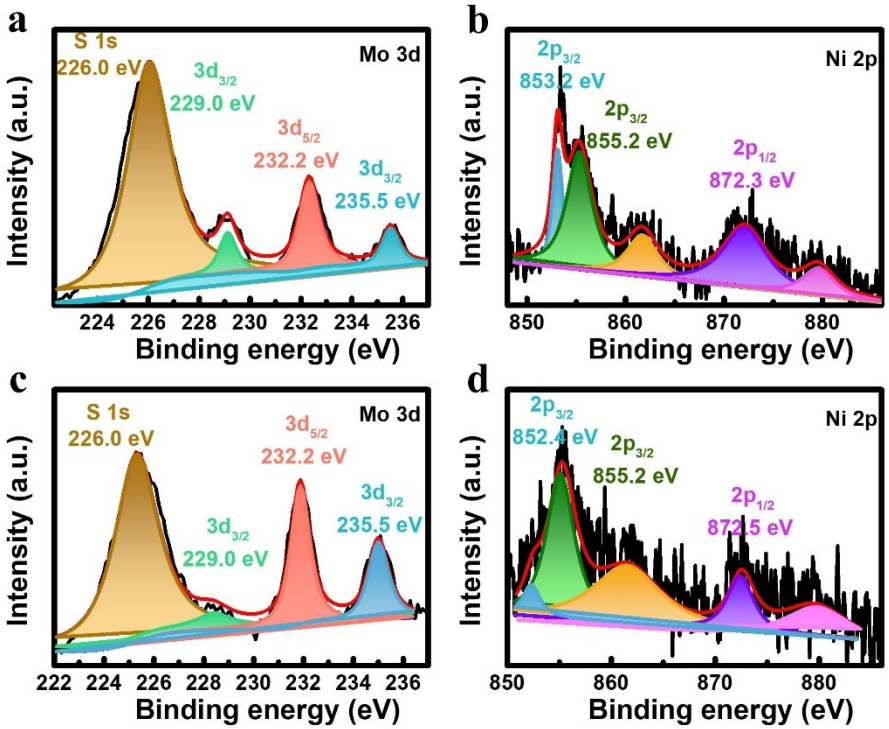

Fig. S12 XPS spectrum of composites with different solvents.

As is shown in **Fig. S12**, it is confirmed that Mo doping and Ni deposition can be achieved in different alcohol solutions, demonstrating the generalizability of the method we developed.

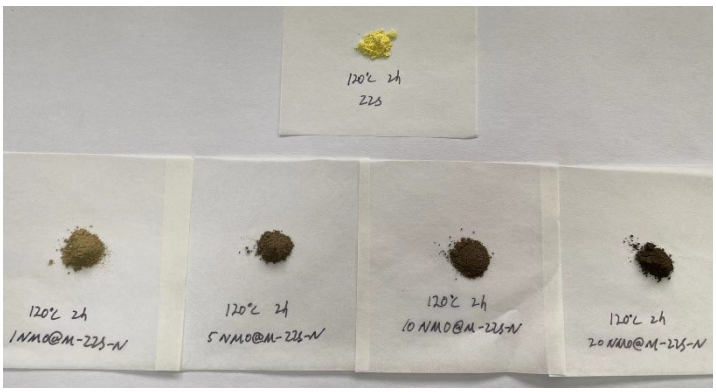

Fig. S13 Optical photos of the synthesized catalysts with increase in the content of $NiMoO_4$.

As shown in **Fig. S13**, the color of NMO@ZIS prepared via different amounts of NMO, becomes significantly darker with the increase of NMO, indicating that the doping density and Ni loading enhance by increasing in the content of NMO.

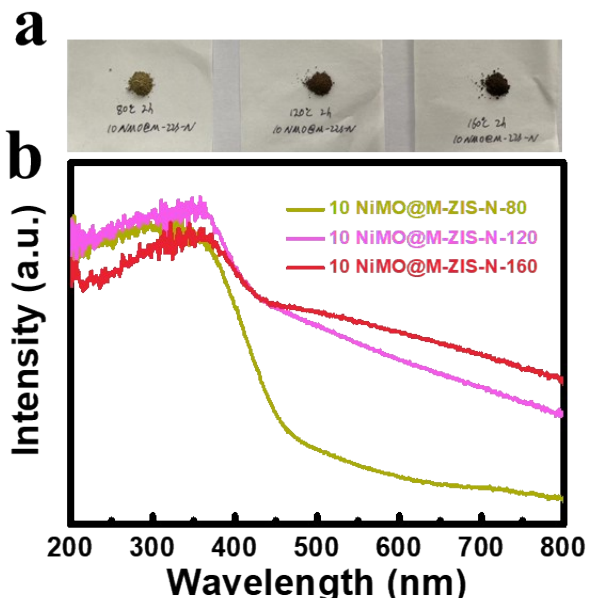

Fig. S14 (a) Optical photos of the synthesized catalysts at different temperatures and corresponding to the (b) UV-vis DRS spectra.

It can be seen from **Fig. S14a** that the color of the catalyst gradually increased with increasing temperature, revealing the significant increase in Mo doping and Ni loading. Moreover, the UV-vis DRS spectra of 10 NMO@M-ZIS-N-X in **Fig. S14b** show the absorption edge of the catalysts gradually red-shifted with the increase of temperature, which is ascribed to the change of those Mo doping and Ni loading.

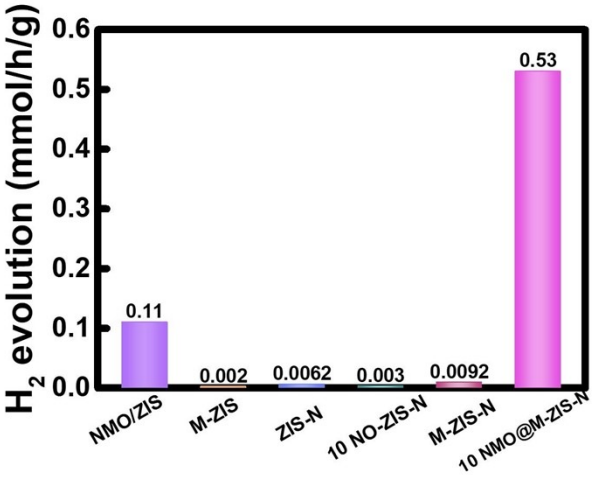

Fig. S15 Photocatalysis HER rate of various photocatalysts with sodium lignin sulfonate as a

sacrificial agent.

The control samples with sodium lignosulfonate as sacrificial agent, was shown in **Fig. S15**. Obviously, compared with 10 NMO@M-ZIS-N, all the comparative samples except NMO/ZIS exhibited dramatically poor photocatalytic reforming lignin activity for hydrogen production. This is because NMO can generate strongly oxidized holes or hydroxyl radicals in NMO/ZIS to oxidize sodium lignosulfonate, while the electrons generated by ZIS reduce protons in water to hydrogen. On the contrary, the doping and metal deposition of Mo cannot effectively enhance the oxidation and reduction ability of ZIS, which cannot effectively oxidize sodium lignosulfonate, leading to the poor photocatalytic hydrogen evolution activity.

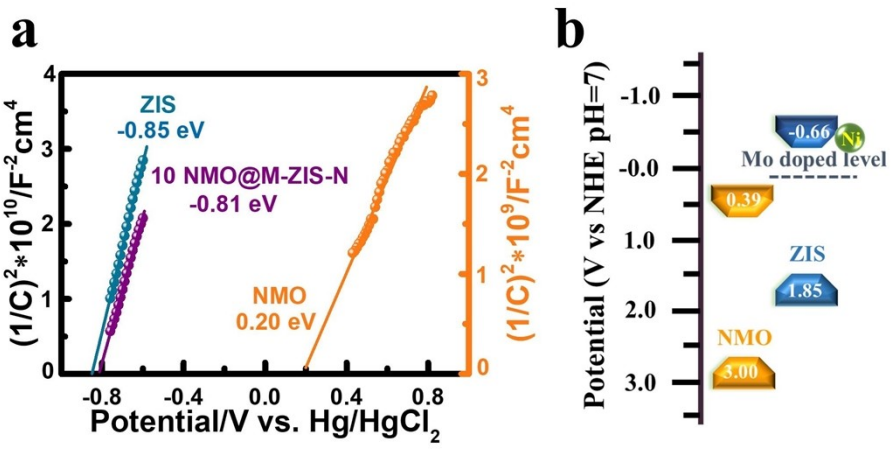

Fig. S16 (a) Mott-Schottky curves of the samples and (b) corresponding band structure.

Calculation of the energy band structure of photocatalytic composites based on different methods:

Based on Tauc plot of the samples and Mott-Schottky curves (Fig. S16a):[2]

$$E_{(vs\,NHE)} = E_{fb} - E_{Hg_2Cl_2} + 0.059 \times pH$$

where $E_{(vs\,NHE)}$: represents the standard hydrogen potential; E_{fb}: represents the flat band potential; $E_{Hg_2Cl_2}$=0.223 V; pH=7.

Based on theoretical calculation:[3]

$$E_{VB} = X - E_e + \frac{1}{2}E_g$$

$$E_{CB} = E_{VB} - E_g$$

where X represents the absolute electronegativity of the semiconductor and E_e represents the free electron energy on the hydrogen scale (4.5 eV).

The calculation results are shown in **Table S1**, which is deviated from our analysis based on Tauc plot of the samples and Mott-Schottky curves. Here we take the experimental results as the standard.

Table S1 Calculation of the energy band structure of photocatalytic composites based on different methods.

	NMO*	ZIS*	NMO$	ZIS$
E_g (eV)	2.61	2.48	2.61	2.48
E_{CB} (eV)	0.39	-0.66	0.37	-0.88
E_{VB} (eV)	3.0	1.85	2.98	1.60

Note：* Based on Mott-Schottky curves; $ Based on theoretical calculation.

Table S2 Hydrogen evolution rates for 10 NMO@M-ZIS-N in this work compared with the reported work related to co-catalyst free photocatalysts.

Samples	Sacrificial agent	Hydrogen production rate (mmol g^{-1} h^{-1})	References
$ZnIn_2S_4/LaNiO_3$	TEOA	1.6	4
$ZnIn_2S_4$@$In(OH)_3$	Solution of Na_2S and Na_2SO_3	2.1	5

g-C_3N_4 nanosheet@$ZnIn_2S_4$	TEOA	2.8	6
$ZnIn_2S_4$-rGO-$CuInS_2$	Solution of Na_2S and Na_2SO_3	0.51	7
$WO_3/ZnIn_2S_4$	Solution of Na_2S and Na_2SO_3	2.2	8
$Ti_3C_2TX/ZnIn_2S_4$	TEOA	3.5	9
RGO/La-$ZnIn_2S_4$	Solution of Na_2S and Na_2SO_3	2.3	10
CdS-$ZnIn_2S_4$	Solution of Na_2S and Na_2SO_3	3.1	11
NH_2-MIL-125(Ti)@$ZnIn_2S_4$/C-dS	MeOH/H_2O	2.4	12
10 NMO@M-ZIS-	TEOA SLS	5.14 0.53	*This work*

References

1. A. Zuliani, A. M. Balu, R. Luque, *ACS Sustain. Chem. Eng.* 2017, **5,** 11584-11587.
2. S. Cao, B. Shen, T. Tong, J. Fu, J. Yu, *Adv. Funct. Mate.* 2018, **28,** 1800136.
3. K. Boriachek, M. N. Islam, A. Moller, C. Salomon, N. T. Nguyen, M. S. A. Hossain, Y. Yamauchi, M. J. A. Shiddiky, *Small*, 2018, **14**, 21.
4. Z. Y. Wang, B. Su, J. L. Xu, Y. D. Hou, Z. X. Ding, *International Journal of Hydrogen Energy*, 2020, **45,** 4113-4121.
5. M. J. Geng, Y. H. Peng, Y. Zhang, X. L. Guo, F. K. Yu, X. L. Yang, G. W. Xie, W. S. Don, C. L. Liu, J. F. Li, J. Q. Yu, *Int. J. Hydrogen Energ.* 2019, **44,** 5787-5798.
6. B. Lin, H. Li, H. An, W. B. Hao, J. J. Wei, Y. Z. Dai, C. S. Ma, G. D. Yang, *Appl. Catal. B-Environ.* 2018, **220,** 542-552.
7. A. Raja, N. Son, M. Swaminathan, M. Kang, *J. colloid interf. sci.*2021, **602,** 669-679.
8. P. F. Tan, A. Q. Zhu, L. L. Qiao, W. X. Zeng, Y. J. Ma, H. G. Dong, J. P. Xie, J. Pan, *Inorg. Chem. Front.* 2019, **6,** 929-939.
9. G. C. Zuo, Y. T. Wang, W. L. Teo, A. M. Xie, Y. Guo, Y. X. Dai, W. Q. Zhou, D. Jana, Q. M. Xian, W. Dong, Y. L. Zhao, *Angew. Chem. Int. Edit.* 2020, **59,** 11287-11292.
10. R. S. Zhu, F. Tian, S. N. Che, G. Cao, F. Ouyang, *Renew. Energ.* 2017, **113,** 1503-1514.
11. Y. W. Zhu, J. Chen, L. H. Shao, X. N. Xia, Y. T. Liu, L. L. Wang, *Appl. Catal. B-Environ.* 2020, **268**.
12. S. Zhang, M. Du, Z. Xing, Z. Li, K. Pan, W. Zhou, *Appl. Catal. B-Environ.* 2020, **262**.